Effect of Tempering Pass on HSLA-80 Steel HAZ Microstructures

Continuous cooling transformation diagrams devised from a simulated thermal cycle were applied over a high-temperature, modified Nb-bearing steel microstructure

BY A. CRUZ-CRESPO, D. BEZERRA DE ARAUJO, AND A. SCOTTI

ABSTRACT

The alloying system and thermal history of the hot rolling process applied to high-strength low-alloy steels (HSLA) leads to a very particular behavior of these materials under welding thermal cycles. In this work, microstructures and hardness of a grain-coarsened heat-affected zone (HAZ) were analyzed from API 5L X80 Nb microalloyed steel specimens after undergoing simulated thermal cycles to represent both first and tempering passes. The first thermal cycle for each sample reached the peak temperature of 1350°C, while the second was of 950°C. Using the different cooling curves imposed by the simulator, a continuous cooling transformation (CCT) diagram was raised for both conditions. The predominant microstructure for the first thermal cycle was granular bainitic ferrite at low cooling rates, but it changed into bainitic ferrite as cooling rate increases, reaching some presence of martensite at the highest cooling rates. The microstructure in the second thermal cycle is quasi-polygonal ferrite at low cooling rates and bainitic ferrite at the fastest cooling rates. However, the hardness did not exceed 300 HV in any case and the hardness measured was even lower in the simulated tempering pass specimens. These results indicate that this steel has high weldability and no special techniques, such as preheating, need to be employed to prevent cold cracking. However, the study suggests the need for future work on aging of precipitates in this grain-refined region due to the tempering pass.

Introduction

Microalloyed steels of high strength and low alloy (HSLA) have an excellent combination of properties (high yield strength, toughness, and weldability) due to their unique characteristics of small grain sizes achieved through very low contents of alloy elements and thermomechanical treatment. Thus, Almeida et al. (Ref. 1), who is also supported by other authors such as Jing-Hong et al. (Ref. 2), refers to the tendency of increasing application of HSLA steels where weight reduction is required (through wall thickness reduction), while ensuring high weldability, which is required for field welding. The trend in the development of these steels for piping (API 5L X-60, X-80, X-100 steel, according to the classification of the American Petroleum Institute) is closely linked to industrial demand for increasing the diameters and work pressure in pipelines.

The continuous improvement in the properties of the HSLA steels has been achieved by the presence of a very low content of alloying elements, such as Nb, Ti, and V, and a thermomechanically controlled treatment during rolling, which (both) contributes to a decrease in grain size. Other important factors, as reported by Jing-Hong et al. (Ref. 2), are the formation of desired microstructures and precipitates (acicular ferrite and bainite, which may also appear with retained martensite/austenite (MA) constituents).

On the other hand, since welding processes are employed in applications using steels from the API 5L class, it is evident that the influence of the thermal cycles on the heat-affected zone (HAZ) microstructures is of vital importance, especially in the region of coarsened grains. This has resulted in a large number of papers focused on the study of this area. Das (Ref. 3) suggested that the refinement of the microstructure near the weld interface is very effective in improving the HAZ toughness of microalloyed steels, which is achieved by delaying the austenite grain growth, with the transformation to acicular ferrite and formation of precipitates or inclusions within the austenite grains. For his part, Moeinifar et al. (Ref. 4) addressed the effect of thermal cycling in X-80 steel, showing that the heat input in the submerged arc welding (SAW) process (leading to different thermal cycles) has a significant influence on the microstructure and hardness of the coarse-grain HAZ. With similar results, Mohandas et al. (Ref. 5) provided a comparative study of the behavior of HAZ microstructure and properties for three steels of different compositions with the shielded metal arc welding (SMAW), gas tungsten arc welding (GTAW), and gas metal arc welding (GMAW) processes, relating the process energy input to the microstructure and properties of the HAZ.

Zhang et al. (Ref. 6) obtained, in a comparative study of two HSLA steels with and without niobium, based on the physical simulation of thermal cycles in a Gleeble simulator, a microstructure with grain boundary ferrite, acicular ferrite, and degenerate pearlite at low cooling rates applied in the no Nb steel specimens, while bainite is formed at fast cooling rates. For the specimens of the Nb-bearing steel, the referred authors obtained granular bainite as a dominant microstructure over a wide range of cooling rates, with martensite appearing at very fast cooling rates. Although for cooling rates slower than 32°C/s, the initial transformation temperature decreases by about 20°C in the presence of niobium. Zhang et al. (Ref. 7), in another article, addressed the

KEYWORDS

High-Strength Low-Alloy (HSLA)
Nb-Microalloyed Steel
Thermal Cycle
Simulation
Heat-Affected Zone (HAZ)
Tempering Pass

A. CRUZ-CRESPO, D. BEZERRA DE ARAUJO, and A. SCOTTI (ascotti@mecanica.ufu.br) *are with the Center for Research and Development of Welding Processes, Federal University of Uberlandia, Brazil.*

Fig. 1 — HSLA microstructure of the Nb microalloyed steel (API 5L X-80).

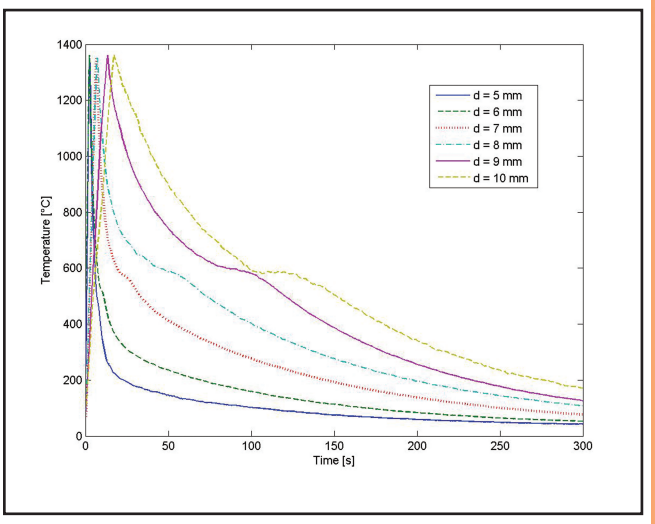

Fig. 2 — Cooling and heating curves experienced by the specimens to simulate the various thermal cycles of the first pass in the region of the coarse grain HAZ (peak temperature = 1350°C) for different diameters of the central part of the specimens: d = 10 mm ($\varphi_{8/5}$ = 3.4°C/s); d = 9 mm ($\varphi_{8/5}$ = 3.8°C/s); d = 8 mm ($\varphi_{8/5}$ = 5.4°C/s); d = 7 mm ($\varphi_{8/5}$ = 13.9°C/s); d = 6 mm ($\varphi_{8/5}$ = 51°C/s); d = 5 mm ($\varphi_{8/5}$ = 126.6°C/s).

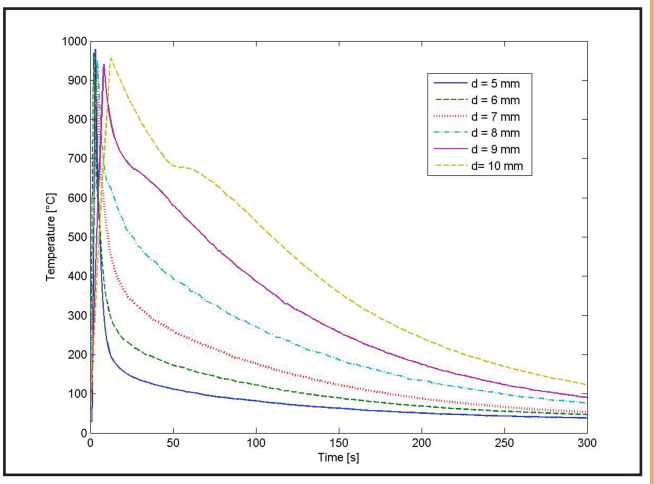

Fig. 3 — Cooling and heating curves experienced by the specimens to simulate the various thermal cycles imposed by the second bead on the region of the coarse-grain HAZ of the precedent bead (peak temperature = 950°C) for different diameters of the central part of the specimens: d = 10 mm ($\varphi_{8/5}$ = 3.7°C/s); d = 9 mm ($\varphi_{8/5}$ = 5.3°C/s); d = 8 mm ($\varphi_{8/5}$ = 15.5°C/s); d = 7 mm ($\varphi_{8/5}$ = 52.2°C/s); d = 6 mm ($\varphi_{8/5}$ = 95.2°C/s); d = 5 mm ($\varphi_{8/5}$ = 151.5°C/s).

effect of niobium on the microstructure, on the coarse-grained HAZ properties, and on the starting transformation temperature under the effect of different energy inputs. Shome (Ref. 8), while also using simulation, established that the peak temperature makes the austenitic grain size increase linearly, influencing the HAZ structure and properties.

While it is true that the effects of the chemical composition and welding energy on the resulting microstructure of the coarse region of the microalloyed steel HAZ have been relatively well studied, specialized literature shows little or no data regarding the effect of the "tempering pass" on the coarse region. The main reason for this is that the coarse-grained region is always of concern in studies on weldability of structural steels, as a region susceptible to loss of toughness and as being a facilitator of hydrogen cracking. The microstructure refined by the "tempering pass" technique is usually quite beneficial for reducing hardenability and increasing toughness. In addition to not being known in detail, the microstructure resulting in the refined region can be expected for steels with higher contents of Nb to present aging of the precipitates. Therefore, the objective of this study was to evaluate the microstructural formation of a tempering pass on the coarse-grained region of the HAZ of Nb microalloyed HSLA-80 steel, through simulating welding thermal cycles from a first pass followed by a tempering pass.

Materials and Methods

The methodology approach of this work was the imposition of thermal cycles representing welding with different energies through simulation on samples of a microalloyed steel of high strength (HSLA), Type API 5L X80, composition being reported in Table 1. The coarse-grained region of the HAZ was initially simulated, assuming a peak temperature of 1350°C and cooling rates ranging from 3° to 130°C/s. Half of the specimens that underwent this simulation were heated again to 950°C to simulate the effect of heat treatment that is carried out by a second bead over the region of the coarse-grained HAZ (CGHAZ) of a precedent bead (tempering pass).

As shown in Fig. 1, the base metal has a microstructure with high prevalence of polygonal ferrite. Alongside the polygonal ferrite, dark-etching regions are present, resulting from transformations of the residual austenite at relatively low temperatures (probably composed of bainite and MA microconstituent). This microstructure pattern coincides with that reported by Jing-Hong et al. (Ref. 2), Cizek et al. (Ref. 9), and Bott et al. (Ref. 10), who deal with the char-

Table 1 — Chemical Composition of the Nb Microalloyed Steel (API 5L X-80), in % Mass

C	Mn	Si	P	S	Mo	Ni	Cr	Cu
0.04	1.71	0.25	0.009	0.004	0.006	0.156	0.202	0.214
V	Nb	Ti	Al	N	B	V + Nb + Ti		
0.003	0.100	0.009	0.018	0.005	0.0001	0.112		

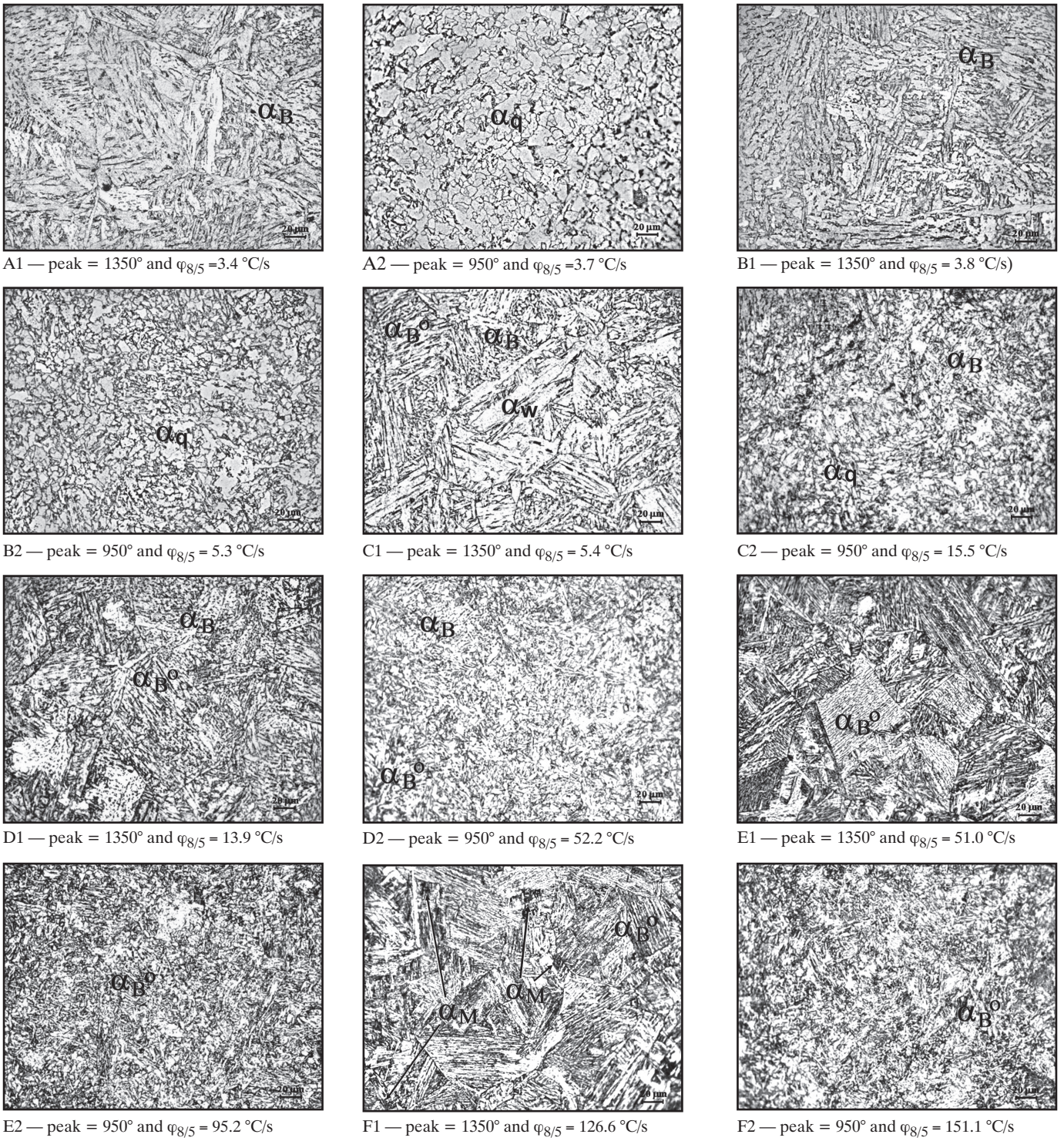

A1 — peak = 1350° and $\varphi_{8/5}$ =3.4 °C/s

A2 — peak = 950° and $\varphi_{8/5}$ =3.7 °C/s

B1 — peak = 1350° and $\varphi_{8/5}$ = 3.8 °C/s)

B2 — peak = 950° and $\varphi_{8/5}$ = 5.3 °C/s

C1 — peak = 1350° and $\varphi_{8/5}$ = 5.4 °C/s

C2 — peak = 950° and $\varphi_{8/5}$ = 15.5 °C/s

D1 — peak = 1350° and $\varphi_{8/5}$ = 13.9 °C/s

D2 — peak = 950° and $\varphi_{8/5}$ = 52.2 °C/s

E1 — peak = 1350° and $\varphi_{8/5}$ = 51.0 °C/s

E2 — peak = 950° and $\varphi_{8/5}$ = 95.2 °C/s

F1 — peak = 1350° and $\varphi_{8/5}$ = 126.6 °C/s

F2 — peak = 950° and $\varphi_{8/5}$ = 151.1 °C/s

Fig. 4 — Corresponding microstructures for the first cycle (A1, B1, C1, D1, E1, F1) and second cycle (A2, B2, C2, D2, E2, F2) with different cooling rates (different specimen diameters), where α_q = quasi-polygonal ferrite, α_B = granular bainitic ferrite, α_B^o = bainitic ferrite, α_W = Widmanstätten ferrite, $\alpha'M$ = martensite [microconstituent nomenclatures based on Krauss and Thompson (Ref. 18)].

acterization of steels of similar composition to the present work. Those authors stated the existence of MA microconstituent associated with the ferritic grain boundaries, which were revealed only under electron microscopy. Other authors, such as Almeida et al. (Ref. 1), Gorni and Mei (Ref. 11), and Shanmugam et al. (Ref. 12), report having found, by means of electron microscopy, some presence of bainite together with ferrite in steels with compositions relatively similar to those shown in Table 1.

These authors associate this fact with the synergistic effect that presents itself for particular relations of microalloying elements. An important group of authors, such as Mishra (Pathak) et al. (Ref. 13) and Moon et al. (Ref. 14), also confirmed the phases and microconstituents already mentioned in the microstructure of steels of similar composition to that in the present study, together with the presence of niobium-rich precipitates associated with the grain boundaries, which undoubtedly contribute to the high mechanical resistance of these steels.

The simulating of the thermal cycling was performed using a simple equipment design (described in Vilarinho and Araujo (Ref. 15)) based on the Joule effect, which

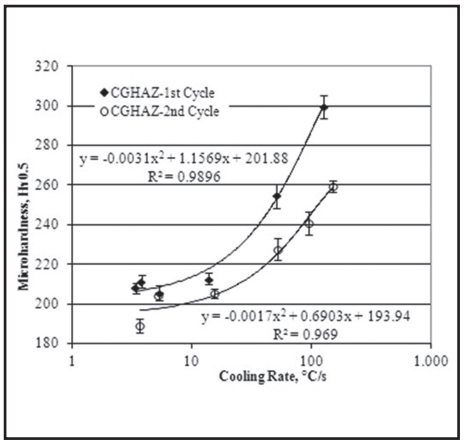

Fig. 5 — Microhardness after both the first and second thermal cycles as a function of the cooling rate between 800° and 500°C.

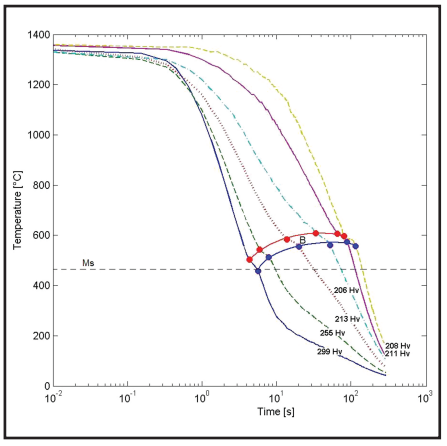

Fig. 6 — CCT diagrams resulting from the first thermal cycle (simulating the coarse-grain HAZ region): The martensite starting temperature (Ms ≈ 465°C) is a predicted value, calculated from Andrews's equation Ms(°C) = 539 – 423 C – 30.4 Mn – 17.7 Ni – 12.1 Cr –7.5 Mo, employed by Zhang et al. (Ref. 7).

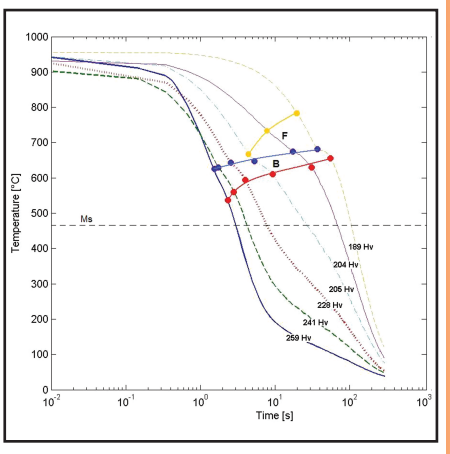

Fig. 7 — CCT diagrams resulting from the second thermal cycle (simulating the refinement of the coarsened-grain region of the HAZ-tempering pass): The martensite starting temperature (Ms ≈ 465°C) is a predicted value, calculated from Andrews's equation Ms(°C) = 539 – 423 C – 30.4 Mn – 17.7 Ni – 12.1 Cr – 7.5 Mo, employed by Zhang et al. (Ref. 7).

enables rapid heating of specimens and allows for natural cooling of the specimens with the aid of aluminum heat sinks that also function as support and electrical contact. An electronic controlling device disconnects the power source when the preregulated temperature at the center of the test pieces is reached. The thermocouple placed in the center of the sample also records the cooling, which due to the small dimensions of the sensor (Type K, diameter 0.5 mm) and the characteristics of continuous natural cooling can detect the starting and finishing points of the metallurgical transformations.

The specimens were cylindrical, 150 mm long, with 10 mm diameter at the extremes. In the central part, along a 10-mm length, different diameters (5–10 mm) were machined, allowing for variances in the cooling rate over a wide range. These geometric measures were determined by the finite element method (Ansys) for the desired cooling rates. One disadvantage of this technique is that in order to obtain very fast cooling rates, the specimen diameter has to be small, and likewise the material volume from which the thermal cycle is measured. This characteristic makes the sensitivity of the method lower to detect activation energy for the starting and finishing of transformations. Cross-sections of the specimens under different cooling rates were cut in the central region for metallographic analysis (2% Nital etching) and microhardness (10 indentations with a load of 500 g and a load application time of 10 s).

To determine the starting and finishing points of the transformations, a differential analysis has been used, as described by Zachrisson (Ref. 16). This analysis consists of performing a regression of a part of the experimental cooling curves (the curve that best fits is the exponential type $T_{reg} = ae^{bt} + ce^{dt}$, where a, b, c, and d are coefficients obtained by regression analysis and where "t" is the time) and extrapolate it so as to include temperatures below transformation. The difference between the thermal cycle experimental curve (T = f(t)) and the regression curve in the region where deviation is perceived ($D(T)_i = T_i - T_{regi}$) is plotted in relation to temperature, thereby obtaining the temperatures of the transformations. A similar technique was successfully applied by Alexandrov and Lippold (Ref. 17), but rather than using determined exponential equations as reference thermal cycles, they used calculated (analytic formulas or numerical modeling) ones for generating the references.

Results and Discussion

Thermal Cycles of the Coarse-Grain Region of the HAZ during the First and Tempering Passes

The curves of thermal cycles to simulate the effect of the first bead (peak temperatures 1350°C) are shown in Fig. 2. Analogously, the thermal cycles to simulate the effect of a second weld pass (peak temperature of 950°C), that is, the overheating of a region affected by the heat of the precedent pass (coarse-grain region of the HAZ, in this case), are shown in Fig. 3. Inflections in the curves shown in Figs. 2 and 3 are observed (more distinct

Table 2 — Resulting Cooling Rates between 800° and 500°C ($\varphi_{8/5}$) that the Specimens Experienced after Heating up to 1350° and 950°C, to Simulate a First Pass and the Subsequent Effect of a Tempering Pass, Respectively, under Different Simulated Heat Inputs

Specimen center diameters (mm)	Cooling rate (°$\varphi_{8/5}$) from first pass CGHAZ simulation	Cooling rate (°$\varphi_{8/5}$) from tempering pass simulation on the CGHAZ
5	126.6°C/s	151.5°C/s
6	51°C/s	92.2°C/s
7	13.9°C/s	52.2°C/s
8	5.4°C/s	15.5°C/s
9	3.8°C/s	5.3°C/s
10	3.4°C/s	3.7°C/s

Note: Cooling rates after heating up to 1350°C to simulate a first pass and then heating the same specimen to 950°C to simulate the effect of a subsequent tempering pass.

for slower cooling rates, justified mainly because of a larger metal volume in the region of temperature measurements and a not high enough dynamic response from the thermocouple — 0.5-mm wires). These are characteristics of the activation energy for the start and finish of the transformation in ferritic steels. The cooling rates ($\varphi_{8/5}$) in the range of temperatures from 800° to 500°C are summarized in Table 2 and also reported in the captions of the thermal cycle plots.

As seen, the cooling rates become proportionately faster for the thermal cycle with peak temperature of 950°C compared to the first cycle with peak temperature of 1350°C. Such behavior is typical of simulations as in the present work (less heat to dissipate), but that should also be observed in an actual welding setting.

Influence of the First and Second Thermal Cycles on the Microstructure of the Coarse Region HAZ

The difference in behavior of the transformations during cooling of the specimens with different cooling rates leads to variations in the microstructure of some with regard to others. (The microstructure identification in this work was based on a nomenclature for ferritic microconstituents taken from the *Atlas for Bainitic Microstructures*, developed by the Iron and Steel Institute of Japan Bainite Committee and described by Krauss and Thompson (Ref. 18).) It is important to mention that microconstituent nomenclature for carbon steel HAZ is still not standardized, but a discussion in this direction or any proposal of microstructure nomenclature is out of focus for this paper. Figure 4 shows, side by side, the microstructures of the specimens under different thermal cycles, at 1350°C (simulating the first pass) on the left, and 950°C (simulating the tempering pass) on the right. In relation to the original microstructure of steel (Fig. 1), one perceives greater grain sizes in the region heated to 1350°C (Fig. 4, left). The grain growth for this type of steel resulting from a range of peak temperatures has been studied by Kuziak et al. (Ref. 19) and Shome (Ref. 8), for whom up to a temperature of about 1100°C the austenite grain practically does not grow, but then increases almost linearly at a high rate. This phenomenon could be motivated by the dissolution of the precipitates rich in Nb as a function of the elapsed time at temperatures above 1100°C. In contrast, Ivanov et al. (Ref. 20) show a gradual growth of the grain at peak temperature.

Figure 4A1 and Fig. 4B1 show the microstructure of the coarse-region HAZ with slow cooling (3.4° and 3.8°C/s), characterized by the predominant presence of granular bainitic ferrite (α_B). This result is consistent with those reported by Zhang et al. (Refs. 6, 7), Gorni and Mei (Ref. 11), and Ivanov et al. (Ref. 20), who obtained CCT diagrams for steels with relatively similar compositions to that of the present work, where the transformation from austenite to bainite is predominant. And for the cooling rate of 5.4°C/s, shown on the microstructure (Fig. 4C1), alongside the granular bainitic ferrite (α_B) there is the presence of bainitic ferrite of type α_B^o and Widmanstätten ferrite (α_W). For even faster cooling rates (13.9° to 51.0°C/s), the presence of bainitic ferrite of type α_B^o is even more visible (Fig. 4D1 and E1). In the case of 4D1, there is still some granular bainitic ferrite α_B. Whenever a peak temperature above the dissolution of the niobium-rich precipitates is reached, which, according to Zhang et al. (Ref. 6) and Moeinifar et al. (Ref. 4), is less than 1200°C, this element (Nb), in solid solution for such cooling rates, obstructs the kinetics of ferrite grain formation. This happens because solute drags at the austenite grain boundary, thereby promoting the formation of bainitic ferrite type α_B^o. In the particular case of the cooling rate of 126.6°C/s, Fig. 4F1 shows the presence of martensite (αM) mixed with bainitic ferrite type α_B^o. The presence of bainitic ferrite (α_B^o) with martensite ($\alpha' M$) in the microstructure at faster cooling rates is consistent with that reported by Zhang et al. (Ref. 6) and Ivanov et al. (Ref. 20), who show a CCT diagram (obtained for a steel composition relatively similar to the present study) with martensitic transformation at lower temperatures when the cooling rate exceeds 50°C/s.

According to the manifestation of a large number of authors, among them Shi and Han (Ref. 21), transformation of austenite to bainite takes place during the cooling process experienced by the different specimens (different cooling rates). This occurs through a migration of carbon into the interior of the austenite grains, thereby stabilizing the austenite and favoring martensite transformation at lower temperatures, which leads to the appearance of MA microconstituent. These authors show that to the extent that $t_{8/5}$ increases (with decreasing cooling rate) the MA fraction increases.

The microstructures corresponding to the coarse region HAZ after undergoing a second thermal cycle with different cooling rates are shown to the right in Fig. 4. The peak temperature reached the normalization temperature (grain refinement) for the steel under study, considering the high heating rates. In all cases, there is a tendency toward the formation of a finer microstructure as compared to the first heat cycle, as would be expected by the thermal history imposed (even considering starting the transformation from coarse grains, the comparison with Fig. 1 shows the grains will be as fine as those of the base metal, suggesting the action of restriction to grain growth of Nb carbonitrides).

If one compares the microstructure of Fig. 4A2, corresponding to the slowest cooling rate of the second thermal cycle, with that of Fig. 1, corresponding to the base metal, a high similarity is noted. This microstructure is characterized by a high predominance of quasi-polygonal ferrite (α_q). In such cases, the most notable difference is that, in the base metal (Fig. 1), the grains have a certain orientation due to the effect of the controlled thermomechanical rolling process and the ferrite grain boundaries are smooth and continuous, in that for the lowest cooling rate in the second cycle (Fig. 4A2) the grains present irregular grain boundaries.

The presence of quasipolygonal ferrite (α_q) is noted in the microstructure after the second cycle at low cooling rates — Fig. 4A2, B2, and C2. In the particular case of 4C2 (cooling rates of 15.5°C/s) alongside the quasipolygonal ferrite (α_q) is the presence of granular bainitic ferrite (α_B). For faster cooling rates (52.2°C/s), the microstructure is granular bainitic ferrite (α_B) mixed with bainitic ferrite type α_B^o — Fig. 4D2. And for cooling rates of 95.2° and 151.2°C/s, the microstructure is predominantly bainitic ferrite (α_B^o) — Fig. 4E2 and 4F2. The fact that no martensite appears in the microstructure (Fig. 4F2), despite a faster cooling rate (151.5°C/s) than in the first cycle (126.6°C/s), is explained, according to Shome and Mohanty (Ref. 22), as the reduction of austenite grain size in the sample under the second thermal cycle, which reduces the hardenability.

The Influence of the First and Second Thermal Cycles on the Microhardness of the Coarse-Region HAZ

The microhardness values obtained for the HAZ grain-coarsened region, corresponding to different cooling rates between 800° and 500°C during the thermal cycles simulating the first bead and the tempering pass, are shown in Fig. 5. It becomes evident that, in general, the microhardness tends to increase with an increase in the cooling rate, which is explained mainly by the modifications undergone in the microstructure, which are covered in detail in the previous section. (The effect of grain sizes on hardness, i.e., a faster cooling rate would lead to smaller grains, which, in turn, usually present greater hardness, cannot be neglected in this analysis, yet with less significance, considering the fact that the found hardness for the tempering pass is lower than that of the first pass, although the temper-

ing grain size is smaller.) Such behavior has been reported by a large number of authors for steels of similar composition to that used in the present work, including such authors as Zhang et al. (Ref. 6), Gorni and Mei (Ref. 11), Cizek et al. (Ref. 9), and Ivanov et al. (Ref. 20), which is obviously also justified based on the changes in the microstructure. In the particular case of Gorni and Mei's work, one obtains the behavior of the Vickers hardness as a function of cooling rate on a logarithmic scale, showing that a steel of lower carbon content (0.04%) hardness is practically constant for low values of cooling rate, growing for faster cooling rates, acquiring a parabolic character, similar to that shown in Fig. 5 of this work.

The microhardness of the base metal (218 ± 5 $HV_{0.5}$) is slightly superior to that obtained after the thermal cycles simulating the first pass with slow cooling rate (208 ± 3 $HV_{0.5}$, 211 ± 3 $HV_{0.5}$, 206 ± 4 $HV_{0.5}$, 213 ± 3 $HV_{0.5}$, corresponding to 3.4°, 3.8°, 5.4°, and 13.9°C/s, respectively — Fig. 5). This fact is more associated with the elapsed time at high temperatures, above the dissolution temperature of the Nb-rich precipitates, than with the cooling rates between 800° and 500°C. After a sufficient elapsed time at high temperatures for dissolution to occur, the cooling rate is such that it prevents the diffusive process and the reprecipitation on the grain boundary, which make a significant hardening effect. The loss of the hardening effect of the precipitates is not fully compensated for by the hardening effect of the transformation, which takes place upon cooling due to the thermal cycle.

Interestingly, the particular case of specimen microhardness under the cooling rate of 5.4°C/s during the first thermal cycle, which although statistically similar to the specimens with slower rates, is slightly lower in terms of its average value. If observed in detail in the microstructure of Fig. 4A1, B1, and C1, one can perceive that, alongside the granular bainitic ferrite (α_B), bainitic ferrite ($\alpha_B{}^o$), and Widmanstätten ferrite (α_W) microstructures appeared in the form of coarse plates for the lowest cooling rate (5.4°C/s), causing a softening. However, it is appropriate to reiterate that the softening of the metal is not significant from the point of view of the statistical value variability.

Zhang et al. (Ref. 6) suggest that the hardness of the granular bainitic ferrite (α_B) ranges between 210 and 240 HV, so the microhardness values obtained for specimens with slower cooling rates (3.4°, 3.8°, 5.4°, and 13.9°C/s) in the first heat cycle (Fig. 5) fully correspond to the presence of granular bainitic ferrite (α_B) observed for these specimens in Fig. 4A1, B1, C1, and D1. For their part, Moeinifar et al. (Ref. 4), who reported the predominance of granular bainitic ferrite (α_B) in the microstructure of the coarse-grained region of the HAZ, obtained microhardness values near the maximum range for this already mentioned microconstituent (around 240 HV). The difference between the microhardness values for granular bainitic ferrite (α_B) obtained by these authors and those obtained in the present work is related to the higher carbon content in the steel for the aforementioned work.

For the highest cooling rates (51.0°C/s and 126.6°C/s) during the first thermal cycle, the growth of the microhardness (Fig. 5) is undoubtedly linked to the high presence of bainitic ferrite ($\alpha_B{}^o$) (Fig. 4E1), bainitic ferrite ($\alpha_B{}^o$), and martensite ($\alpha'M$) — Fig. 4F1. Such an increase in the microhardness together with an increase in the cooling rate could also be related to increasing the volume fraction of the MA microconstituent. As such, Moeinifar et al. (Ref. 4) concluded that increasing the cooling rate increases the fraction of the MA microconstituent, which, in this case, plays a governing role on the hardness progress in the region of the coarse grain in the HAZ.

Zhang et al. (Ref. 6) state that martensite ($\alpha'M$) presents microhardness values of 320 to 340 HV, which were not reached in this work, even for the highest cooling rate (126.6°C/s) during the first thermal cycle — Fig. 5. Ivanov et al. (Ref. 20) declared the presence of martensite for high cooling rates, obtaining a microhardness value of around 325 HV at 50°C/s, when the peak temperature is 1350°C. Such a high value in microhardness obtained by the above authors, in relation to this work, is primarily related to the higher carbon content (0.06%) compared to that reported in Table 1.

From Fig. 5, the second thermal cycle (simulated tempering pass) also leads to an increased microhardness as the cooling rate is faster, consistent with the modifications undergone in the microstructure (Fig. 4A2–F2). Such an increase in the microhardness could also be related to the possible increase in the volume fraction of the MA microconstituent. When comparing microhardness as a function of cooling rate between conditions after the first cycle and after the second cycle, it is clear that there is regularity in behavior between the two conditions, but lower values for the second thermal cycle (the difference becomes more evident as the cooling rate increases). The parabolic character obtained for the microhardness, both after the first thermal cycle and the second, is completely coincident with results obtained by Gorni and Mei (Ref. 11). The decrease in microhardness is a general indication that the second thermal cycle has a positive effect on the coarse-grained HAZ region. This confirms the reduction of hardenability due to the finer granularity achieved in the recrystallization zone of the coarse HAZ under the second cycle.

Obtaining Continuous Cooling Transformation (CCT) Curves for the First and Second Thermal Cycles of the Coarse-Region HAZ

After thermal cycling of Figs. 2 and 3, the continuous cooling transformation diagrams referring to the first and the second thermal cycles were obtained, as seen in Figs. 6 and 7. In Fig. 6, it can be seen that the changes during the first thermal cycle occur at temperatures lower than those reported by several authors for API X80 steels, amongst them Zhang and Farrar (Ref. 23), Zhao et al. (Ref. 24), Stalheim et al. (Ref. 25), Cizek et al. (Ref. 26), Jing-Hong et al. (Ref. 2), and Liu et al. (Ref. 27). However, these authors have worked with diagrams related to thermal treatment processes, from which it follows that the heating is slower and with longer elapsed time in the austenitic region. This drop in temperature of phase transformation in the case of thermal cycles of the HAZ has been reported by Zhang et al. (Ref. 6). Zhang et al. also showed that as one increases the cooling rate there is a further decrease in the transformation temperature, due to lower elapsed times above 900°C, limiting the diffusive processes of phase transformation. According to Zhang et al. (Ref. 6), and Gorni and Mei (Ref. 11), as the cooling rate between 800° and 500°C grows there is also an improvement in the stability of the austenite, which lowers the transformation temperature.

In total agreement with the CCT diagram of Fig. 6, the curves of Fig. 2 suggest that diffusional transformations (austenite to bainite) take place for any cooling rate (manifested by sensitive variation of latent heat, causing deflection in the recorded thermal cycle). As observed in Fig. 2, deflections were not observed only in the curve of the fastest cooling rate. Latent heat of austenite to martensite transformation is not well divulged in current literature. Radaj (Ref. 28, p. 292) cites other sources to say that the latent heat of the austenite-pearlite transformation is 92 J/g and the latent heat of the austenite-martensite transformation is 83 J/g for a 1.2% C. Even considering the higher content of C and no data provided for austenite-bainite transformation, the differences in the figure are not remarkable to eliminate the deflection. In addition, Alexandrov and Lippold (Ref. 17) detected this transformation measuring in-situ weld metal continuous cooling transformation. Thus, the main reason for not detecting the latent heat of an austenite to martensite transformation in

the cooling curves might be the limitation of the simulation (low metal volume in the region of temperature measurements and not too fast dynamic response from the thermocouple).

Upon analysis of microstructure resulting from transformations (Fig. 4A1–F1), the presence of bainite is declared in all specimens (coarse HAZ during the first thermal cycle). This result is also coincident with those reported by Zhang et al. (Ref. 6), Gorni and Mei (Ref. 11), and Ivanov et al. (Ref. 20), who obtained CCT diagrams for steels of relatively similar composition to the present work, where the transformation from austenite to bainite was predominant. The presence of martensite ($\alpha'M$), (Fig. 4F1) evidenced by hardness close to 300 HV and by the martensite starting temperature line in Fig. 6, may be possible if together with bainitic ferrite (α_B^o) in the microstructure, the curve deflection is still present. This is consistent with that reported by Gorni and Mei (Ref. 11) and Zhang et al. (Ref. 6) for steels similar to the one in this work. From these authors, the martensitic transformation defined is based either on the microstructure and hardness, in the case of Zhang et al. (Ref. 6), or established in calculated (predicted) CCT diagrams, as in the case of Gorni and Mei (Ref. 11) at a constant temperature. For their part, Ivanov et al. (Ref. 20) also obtained a CCT diagram that shows the martensitic transformation temperature for high cooling rates, without declaring how they define this temperature. Zhang et al. (Ref. 6) and Ivanov et al. (Ref. 20) show the martensitic transformation as being possible when the cooling rate exceeds 50°C/s, which is in line with the present work. If one compares the CCT diagram representing the coarse-grain HAZ as for the first pass (Fig. 6) with that obtained according to the second thermal tempering pass cycle (Fig. 7), one can see that in this last mentioned there also appears a transformation of austenite to ferrite curve at low cooling rates, which obviously occurs with a higher level of diffusion. Data from Gorni and Mei (Ref. 11) coincide with this result, which states the ferrite transformation at low cooling rates, below 0.5°C/s. The difference in cooling rates at which this transformation occurred in the referred work and in this present work may be linked to a high retention in the austenite region, which undoubtedly increases the stability of this phase. Also, Ivanov et al. (Ref. 20) agree with the possible occurrence of ferrite transformation, while reporting a CCT diagram where this transformation is reflected even at cooling rates above 50°C/s, which could be associated primarily with higher carbon content (0.06%) in relation to that of the present work (0.04%).

Bainitic transformation for the second thermal cycle (tempering pass) (Fig. 7) occurs at higher temperatures than in the first — Fig. 6. The foregoing is also related to the elapsed time in the austenitic region. In the first cycle, there is more time spent in the austenitic region than in the second due to a higher peak temperature (1350°C for the first cycle and 950°C for the second) leading to increased solubility and slow transformation temperatures during cooling. The presence of martensite in the tempering pass would not be possible within the cooling range under investigation (Fig. 7), which agrees with the microstructures obtained — Fig. 4.

It is important to point out that Andrews's equation for MS temperature prediction used in Figs. 6 and 7 was not developed for steels with such a low-C content. However, Capdevila (Ref. 29) points out that although the relationship between the martensite start transformation temperature and steel composition has been investigated previously by several researchers (for instance, Grange and Stewart, 1946; Payson and Savage, 1944; and Kung and Rayment, 1978), it was the study by Andrews (1965) that has proved to be the most reliable, because it considered the largest number of samples. Sourmaila and Garcia-Mateo (Ref. 30) show a comparison between their proposed neutral network model results and the predictions from Andrews and concluded that the neural network model performs at least equally as well as the thermodynamic approach. Applying Sourmaila and Garcia-Mateo's model for the steel of this work, a very similar MS temperature was found, i.e., 460°C.

General Discussion

Considering the different behaviors between metallurgical characteristics (microstructure and hardness) when applied to a first cycle peak temperature of 1350°C and a second cycle on the coarse-grained zone formed (peak temperature of 900°C), this can be explained by the theory and supported by results from other authors, demonstrating the validity of the applied simulation. The possibility of working with natural cooling in the region of study and application of the technique of differential analysis made it possible to draw up CCT diagrams for different thermal experiences undergone by the steel, similar to what happens in welding.

The CCT diagrams show that for the microstructure of the coarse-grained HAZ zone, either the primary formation (simulating the first pass) or recrystallization (simulating a second pass or tempering pass) are mainly granular bainitic ferrite (α_B) or bainitic ferrite (α_B^o). There is a perceived improvement in properties of the coarse HAZ region when tempered by reducing the grain size and decrease in hardness (the hardenability is lower), showing that the steel in question also has high weldability. From the standpoint of hardness, which according to Ivanov et al. (Ref. 20) has a direct relationship with the mechanical properties for HSLA steels, only a very high cooling rate, greater than 100°C/s, puts the union at risk due to hydrogen-assisted cold cracking initiated in the HAZ. That is, the material could be welded by a very large range of processes and parameters, and no preheating procedure is needed.

Continuous cooling transformation diagrams could be obtained for other regions of the HAZ (including HAZ in the bead metal recrystallized by precedent passes), facilitating the programming of sequences of passes to optimize the joint properties. On the other hand, although it was not verified in the work, carbonitride precipitates or the forming of microconstituent MA could happen, especially in HAZ regions in which the temperature was below the dissolution temperatures for Nb-bearing precipitates. These microconstituents can deteriorate properties of the HAZ, especially concerning toughness. This means that, despite the high weldability demonstrated by this study for this steel, further investigation on all regions of the HAZ is advised and possible with the same experimental approach.

Conclusions

1. The system used to evaluate the effect of thermal cycling on the microstructure formation of the HAZ of a HSLA steel (simulator and method of differential analysis of cooling curve) was effective and practical, sensitive enough to produce CCT diagrams of different regions of the HAZ.

2. For the CCT diagrams of the original HAZ (the first heat cycle) of the steel under study, the microstructure is predominantly granular bainitic ferrite (α_B) at low cooling rates, but is transformed into bainitic ferrite (α_B^o), to the extent that increases in the cooling rate made it finer. Even for very high cooling rates, the microstructure is predominantly bainitic ferrite (α_B^o) with the presence of martensite. In all cases, the microhardness is less than 300 HV, qualifying the steel studied as of good weldability.

3. From the point of view of the basic microstructure, the CCT diagram shows that the recrystallized region (simulating the temperature for a second pass) further improved the weldability of the material under study, by refining the grain while reducing the hardness, even though not significantly altering the type of microstructure.

Acknowledgments

The authors thank engineers Lucia Basilio P. de Souza and Ivy Jorge Franco for their support in performing the thermal simulation of the specimens. They also are pleased to thank the Brazilian agency CAPES, which, by means of project No. 059/2009, financially supported the experimental work and enabled interaction between the researchers involved.

References

1. Almeida, D. M., Maciel, T. M., and Bracarence, A. Q. 2004. ZTA fracture comparative study of bainitic and pearlitic API steel after implant test. *Soldagem & Inspeção* 9(4): 198–204 (ISSN 0104-9224 printed/ISSN 1980-6973 online) (in Portuguese).

2. Jing-Hong, Y., Qing-You, L., Dong-Bai, S., and Xiang-Yang, L. 2010. Microstructure and transformation characteristics of acicular ferrite in high niobium-bearing microalloyed steel. *Journal of Iron and Steel Research, International* 17(6): 53–59.

3. Das, A. K. 2010.The present and the future of line pipe steels for petroleum industry. *Materials and Manufacturing Processes* 25(1-3): 14–19 (DOI: 10.1080/10426910903202427).

4. Moeinifar, S., Kokabi, A. H., and Madaah Hosseini, H. R. 2011. Role of tandem submerged arc welding thermal cycles on properties of the heat-affected zone in X80 microalloyed pipe line steel. *Journal of Materials Processing Technology* 211(3): 368–375 (doi:10.1016/j.jmatprotec.2010.10.011).

5. Mohandas, T., Madhusudan, R. G., and Kumar, B. S. 1999. Heat-affected zone softening in high-strength low-alloy steels. *Journal of Materials Processing Technology* 88(1-3): 284–294 (doi:10.1016/S0924-0136(98)00404-X).

6. Zhang, Y. Q., Zhang, H. Q., Liu, W. M., and Hou, H. 2009(a). Effects of Nb on microstructure and continuous cooling transformation of coarse grain heat-affected zone in 610 MPa class high-strength low-alloy structural steels. *Materials Science and Engineering A* 499, p. 182–186.

7. Zhang, Y. Q., Zhang, H. Q., Li, J. F., and Liu, W. M. 2009(b). Effect of heat input on microstructure and toughness of coarse grain heat-affected zone in Nb microalloyed HSLA steels. *Journal of Iron and Steel Research, International* 16(5), p. 73–80 (doi:10.1016/S1006-706X(10)60014-3).

8. Shome, M. 2007. Effect of heat-input on austenite grain size in the heat-affected zone of HSLA-100 steel. *Materials Science and Engineering A*, p. 454–460.

9. Cizek, P., Wynne, B. P., Davies, C. H. J., Muddle, B. C., and Hodgson, P. D. 2002. Effect of composition and austenite deformation on the transformation characteristics of low-carbon and ultralow-carbon microalloyed steels. *Metallurgical and Materials Transactions A* 33(5): 1331–1349 (doi: 10.1007/s11661-002-0059-8).

10. Bott, I. S., De Souza, L. F. G., Teixeira, J. C. G., and Rios, P. R. 2005. High-strength steel development for pipelines: a Brazilian perspective. *Metallurgical and Materials Transactions A* Vol. 36A, p. 443–454 (ISSN 1073-5623 Printed/ISSN 1543-1940 Online) (10.1007/s11661-005-0315-9).

11. Gorni, A. A., and Mei, P. R. 2004. Austenite transformation and age hardening of HSLA-80 and ULCB steels. *Journal of Materials Processing Technology*, Vol. 155–156, p. 1513–1518 (doi:10.1016/j.jmatprotec.2004.04.245).

12. Shanmugam, S., Ramisetti, N. K., Misra, R. D. K., Hartmann, J., and Jansto, S. G. 2008. Microstructure and high strength–toughness combination of a new 700 MPa Nb-microalloyed pipeline steel. *Materials Science and Engineering A*, 478 (1-2): 26–37 (doi:10.1016/j.msea.2007.06.003).

13. Mishra (Pathak), S. K., Ranganathan, S., Das, S. K., and Das, S. 1998. Investigation on precipitation characteristics in a high strength low alloy (HSLA) steel. *Scripta Materialia* 39(2): 253–259.

14. Moon, J., Kim, S., Lee, J., Hwang, B., Lee, Ch. G., and Lee, Ch. 2008. Effect of Cu and B addition on tempering behavior in the weld CGHAZ of high strength low alloy plate steel. *Materials Science and Engineering A* 497 (1-2): 153–159 (doi: 10.1016/j.msea.2008.06. 031).

15. Vilarinho, L. O., and Araujo, D. B. 2010. Low-cost methodology for obtaining CCT welding diagrams. *Soldagem & Insp.* 15(3): 184–190 (doi:10.1590/S0104-92242010000300004) (in Portuguese)

16. Zachrisson, J. 2006. *In-Situ Detection and Characterization of Phase Transformations in Weld Metals*. Master's thesis. Master of Science Programme, Engineering Physics. Lulea University of Technology, p. 44.

17. Alexandrov, B. T., and Lippold, J. C. 2005. *In-Situ Weld Metal Continuous Cooling Transformation Diagrams*. IIW Doc. IX-2162-05.

18. Krauss, G., and Thompson, S. W. 1995. Ferritic carbon microstructures in steels. *ISIJ International*. Vol. 35 (8), pp. 937–945. Iron and Steel Institute of Japan Bainite Committee, 1992. *Atlas for Bainitic Microstructures*, Vol. 1, ISIJ, Tokyo, pp. 4, 5.

19. Kuziak, R., Botd, T., and Yi-Wen, Ch. 1995. Microstructure control of ferrite-pearlite high strength low alloy steels utilizing microalloying additions. *Journal of Materials Processing Technology*, Vol. 53, p. 255–262 (*http://dx.doi.org/10.1016/0924-0136(95)01983-L*).

20. Ivanov, A. Yu., Sulyagin, R. V., Orlov, V. V., and Kruglova, A. A. 2011. Structure and properties of weld joints in X80, X90, and K70 pipe steel. *Steel in Translation* 41(7): 611–616 (doi: 10.3103/S0967091211070047).

21. Shi, Y., and Han, Zh. 2008. Effect of weld thermal cycle on microstructure and fracture toughness of simulated heat-affected zone for a 800 MPa grade high strength low alloy steel. *Journal of Materials Processing Technology* 207 (1-3): 30–39 (doi:10.1016/j.jmatprotec.2007.12.049).

22. Shome, M., and Mohanty, O. N. 2006. Continuous cooling transformation diagrams applicable to the heat-affected zone of HSLA-80 and HSLA-100 steels. *Metallurgical and Materials Transactions A* 37(7): 2159–2169 (doi: 10.1007/BF02586136).

23. Zhang, Zh., and Farrar, R. A. 1995. *An stlas of Continuous Cooling Transformation (CCT) Diagrams Applicable to Low Alloy Weld Metals.* The Institute of Materials, p. 95.

24. Zhao, M. C., Yang, K., Xiao, F. R., and Shan, Y. Y. 2003. Continuous cooling transformation of underformed and deformed low carbon pipeline steels. *Materials Science and Engineering A* 355(1-2): 126–136 (doi:10.1016/S0921-5093(03)00074-1).

25. Stalheim, D. G., Barnes, R., Keith, E., and McCutcheon, B. 2007. Alloy designs for high strength oil and gas transmission linepipe steel. *International Symposium on Microalloyed Steel for the Oil and Gas Industry*. Eds. W. J. Fazackerley, P. Bordignon, K. Hulka, and F. Siciliano. TMS (The Minerals, Metals & Materials Society), p. 73–108.

26. Cizek, P., Wynne, B. P., Hodgson, P., and Muddle, B. C. 2005. Effect of simulated thermomechanical processing on the transformation characteristics and microstructure of an X80 pipeline steel. *The 1st International Conference on Super-High Strength Steels.* Associazione Italiana di Metallurgia, Italy (ISBN 8885298567).

27. Liu, Ch., Wang, D. Z., Liu, Y. X., Zhu, Q. H., and Zhau, Yu. 1997. Composition design of a new type low-alloy high-strength steel. *Materials & Design* 18(2): 53–59 (doi:10.1016/S0261-3069(97)00029-0).

28. Radaj, D. 2003. *Welding Residual Stresses and Distortion — Calculation and Measurement*, English Edition, Vol. 2, Düsseldorf, DVS-Verlag.

29. Capdevila, C. 2012. Chapter 15: Neural networks modeling of phase transformations in steels. *Phase Transformations in Steels*, Vol. 2: Diffusionless transformations, high strength steels, modelling and advanced analytical techniques. Edited by Elena Pereloma and David V. Edmonds, Woodhead Publishing Ltd., pp. 464–500, ISBN 978-1-84569-971-0 (print)/ISBN 978-0-85709-611-1 (online).

30. Sourmaila, T., and Garcia-Mateo, C. 2005. Critical assessment of models for predicting the Ms temperature of steels. *Computational Materials Science* 34(4): 323–334, *http://dx.doi.org/10.1016/j.commatsci.2005.01.002.*